

The British University in Egypt

BUE Scholar

Basic Science Engineering

Engineering

2022

SCIENTIFIC BREAKDOWN OF A FERROMAGNETIC NANOFUID IN HEMODYNAMICS: ENHANCED THERAPEUTIC APPROACH

M. M. Bhatti

Sara Abdelsalam

Follow this and additional works at: https://buescholar.bue.edu.eg/basic_sci_eng



Part of the [Dynamic Systems Commons](#), and the [Ordinary Differential Equations and Applied Dynamics Commons](#)

SCIENTIFIC BREAKDOWN OF A FERROMAGNETIC NANOFLUID IN HEMODYNAMICS: ENHANCED THERAPEUTIC APPROACH

M.M. BHATTI¹ AND SARA I. ABDELSALAM^{2,3,*} 

Abstract. In this article, we examine the mechanism of cobalt and tantalum nanoparticles through a hybrid fluid model. The nanofluid is propagating through an anisotropically tapered artery with three different configurations: converging, diverging and non-tapered. To examine the rheology of the blood we have incorporated a Williamson fluid model which reveals both Newtonian and non-Newtonian effects. Mathematical and physical formulations are derived using the lubrication approach for continuity, momentum and energy equations. The impact of magnetic field, porosity and viscous dissipation are also taken into the proposed formulation. A perturbation approach is used to determine the solutions of the formulated nonlinear coupled equations. The physical behavior of all the leading parameters is discussed for velocity, temperature, impedance and streamlines profile. The current analysis has the intention to be used in therapeutic treatments of anemia because cobalt promotes the production of red blood cells since it is a component of vitamin B12, this is in addition to having tantalum that is used in the bone implants and in the iodinated agents for blood imaging due to its long circulation time. Moreover, in order to regulate the blood temperature in a living environment, blood temperature monitoring is of utmost necessity in the case of tapering arteries. The management and control of blood mobility at various temperatures may be facilitated by the presence of a magnetic field. The current findings are enhanced to provide important information for researchers in the biomedical sciences who are attempting to analyze blood flow under stenosis settings and who will also find the knowledge useful in the treatment of various disorders.

Received September 24, 2021. Accepted October 16, 2022.

1. INTRODUCTION

Magnetic nanoparticles are very leading material for a variety of biological fields. Particularly, the heat generated by these molecules in a magnetic AC field can be exploited for local hypothermia in tumor treatments [34]. The most basic way is to implant aqueous solutions of these particles directly into the tumors before introducing the field [19]. Platinum has always worked as a catalyst to hydrogen fuel cells but the greatest con in using it is its cost that has been an economic challenge. In recent years, a novel catalyzed material based on the

Keywords and phrases: Hybrid nanofluid, cobalt & tantalum nanoparticles, arterial blood flow, magnetic field, williamson fluid.

¹ College of Mathematics and Systems Science, Shandong University of Science and Technology, Qingdao 266590, Shandong, China.

² Instituto de Ciencias Matemáticas ICMAT, CSIC, UAM, UCM, UC3M, Madrid 28049, Spain.

³ Basic Science, Faculty of Engineering, The British University in Egypt, Al-Shorouk City, Cairo 11837, Egypt.

* Corresponding author: sara.abdelsalam@bue.edu.eg

metal cobalt has been developed as an alternative to platinum, potentially allowing the production of inexpensive and more lasting hydrogen fuel cells. Cobalt is believed to be the first metallic catalyst with capabilities similar to those of platinum [28]. Baldi *et al.* [3] developed different sizes of cobalt ferrite nanoparticles ranging from 5 to 7 nm where they discovered a compound that allows them to fine-tune the average particle size to improve heat release capabilities at a particular frequency across a wide range. In 2016, Tabish *et al.* [31] investigated the *in-vivo* biocompatibility of the nanoparticles of the cobalt iron oxide using a conventional emulsion method. They found that at the applied dosage, the chemical compound under consideration has low biocompatibility and greater cytotoxicity levels in biological systems. The magnetic characteristics of some magnetic particles of different sizes have been investigated by Moumen *et al.* [16]. They discovered a reduction in the coercivity of the particle as a result of the decrease in the diameter of particles from 5 to 2 nm. Nevertheless, the coercivity has a great impact on cobalt ferrite in mechanical systems as investigated thoroughly by Ponce *et al.* [21]. The superparamagnetism of the cobalt ferrite was further studied by Ngo *et al.* [20] in 1999 where it was found that the magnetization is greater for uncoated material than the others. Tung *et al.* [32] experimentally investigated the magnetic characteristics for the ultrafine cobalt ferrite particles where it was found that the system's anisotropy is uniaxial, which is attributed to the involvement of intrinsic strain.

Another type of metallic nanoparticles that has very unique properties in terms of size and structural features is the tantalum nanoparticle. Tantalum is a suitable choice when great corrosion resistance is required. While tantalum is not a refined metal, it is comparable in terms of resistance. Tantalum nanoparticles are also readily oxidized in the air due to their high activity. Planar tantalum is a known clinical metal in the laboratories because of its extremely high biocompatibility which is equivalent to that of other pharmaceutical metallic materials [14]. As a result, it is vital to widen the scope of tantalum's biological uses. In 2017, Schoon *et al.* [29] shed some light on the usage of porous tantalum in hips arthroplasty highlighting the fact that other alloys, that includes cobalt, were initially used in setups of artificial joints. The porosity of tantalum was further emphasized by Mohandas *et al.* [15] in bone reconstructions and regenerative medicine in order to avoid the corrosion that happens due to the involvement of foreign body in the tissues. It was found that the porous tantalum also promotes soft tissue regeneration, including the creation of capillaries, which were discovered to congregate on the surface and inside the geometry of the porous tantalum. It has been seen that hybrid nanoparticles have been utilized widely in order to overcome the shortcomings of single-component nanoparticles, to boost functions and to achieve specific effects for single nanoparticle. The tantalum carbide nanoparticle was, therefore, researched by Ren *et al.* [26] along with cobalt and other metal dopants in 2021 where it was concluded that they provide a promising potential in the modification of the mechanical and catalytic characteristics of ceramic materials. Zhang *et al.* [35] conducted an *in vitro* study to observe the oxidative stress and cytotoxicity of tantalum on macrophages. They concluded that tantalum-based implants may create a more suitable biological environment and have a lower risk of contributing to aseptic loosening when used in the replacement of total joints.

It is commonly understood that physiological fluids, including blood, act generally as non-Newtonian fluids [2, 4, 37]. Many rheological systems have been presented based on the varied rheological properties of non-Newtonian fluids [1, 27]. Non-Newtonian fluid theory is given more consideration than Newtonian fluid analysis due to the enormous technical applications such as emulsifiers, oils, bio-fluids in living tissues and therapeutic fluids. Nadeem and Akram [18] investigated the peristalsis of a Williamson fluid model through an inclined conduit with magnetic field. They concluded that the magnetic field reduces the size of trapped bolus. Prakash *et al.* [22] studied the rheological properties of Williamson fluid in a blood flow through a microchannel with elastic walls. They also took a uniform magnetic field into consideration where they deduced that it enhances the axial velocity in the vicinity of the flexible walls. Hayat *et al.* [9] researched the mass and heat transfer of an incompressible Williamson model with slip condition *via* symmetric channel. They observed that the slip parameter accelerates the flow, unlike the effect of Hartmann number that was seen to decelerate it. Subbarayudu *et al.* [30] numerically assessed the thermophoresis and Brownian diffusion for a Williamson fluid with magnetic field and radiation over a wedge. They found out that as the radiation parameter increases, the temperature is enhanced. Malik and Salahuddin [13] reported the MHD Williamson model with the boundary layer approach. The model was solved using Runge-Kutta-Fehlberg method along with the shooting method where they deduced that the Williamson parameter decelerates the flow. Last but not least, Raza *et al.* [25] evaluated the impact of

linear thermal radiation on a Williamson model through a stretchable sheet using the shooting algorithm and Runge-Kutta-4. They concluded that the Williamson parameter enhances the thermal profile.

Influenced with the above discussion, our target is to investigate the influential effects of cobalt and tantalum nanoparticles embedded in a blood-like fluid presented by a Williamson model through an anisotropically tapered artery. Three different geometries are examined: converging, diverging and non-tapered arteries. The lubrication approach is used to derive the physical and mathematical formulations whereas the perturbation technique is used to derive the appropriate solutions of the governing model. And last, the physical interpretation of the impact of leading parameters are discussed with the physical variables of interest. The current investigation is sought to be useful in the clinical applications where tantalum is employed as a nanoparticle that is readily oxidized in the air due to its high reactivity, and in the treatment of microbial infections since cobalt nanoparticles is nontoxic at lower levels and has less side effects than antibiotics [33].

2. MATHEMATICAL AND PHYSICAL MODELING OF THE BLOOD FLOW

Consider a finite tube having length L filled with non-Newtonian Williamson fluid transporting through a porous anisotropically tapered stenosed artery. The Williamson fluid model is contemplated to examine the rheology of the blood. The fluid contains cobalt and tantalum nanoparticles. The fluid is electrically conducting under the presence of external magnetic field with constant density features. We have used the cylindrical polar coordinates (r, θ, z) , *i.e.*, r, θ are located towards the radial and the circumferential direction, while z is located along the axis of the artery (see Fig. 1). The effects of heat transfer is also shown by taking \tilde{T}_1 at the wall of the artery.

The mathematical expression for the anisotropically tapered artery is defined as

$$\frac{R(z)}{R_0} = \begin{cases} t_v \left(R_0 + \tau z - \frac{\delta \cos \vartheta}{\lambda_0} \left\{ 11 - \frac{94(z-d)}{3\lambda_0} + \frac{32(z-d)^2}{\lambda_0^2} - \frac{32(z-d)^3}{\lambda_0^3} \right\} \right); & d \leq z \leq \frac{3}{2}\lambda_0, \\ t_v (1 + \tau z); & \text{otherwise} \end{cases} \quad (2.1)$$

where δ denotes the stenosis height, $R(z)$ is the tapered arterial segment and the artery radius with composite stenosis, λ_0 represents the stenosis length, t denotes the time, R_0 denotes the normal artery radius in the non-stenotic zone, ϑ is the tapering angle and $\tau = \tan \vartheta$ represents the slope of the tapered vessel. That is, $\vartheta < 0$ shows the converging behavior of artery, $\vartheta = 0$ shows the non-tapered behavior of the artery, whereas $\vartheta > 0$ shows the diverging behavior of the artery. The time variant t_v is described as

$$t_v = 1 + \alpha e^{-\alpha \omega t} (1 - \cos \omega t), \quad (2.2)$$

where ω represents the radial frequency of the forced oscillation and α represents a constant value.

The equations governing the flow model can then be written as [7, 17]

$$\nabla \cdot \tilde{\mathbf{V}} = 0, \quad (2.3)$$

$$\rho_{hnf} \left(\frac{\partial \tilde{\mathbf{V}}}{\partial t} + \tilde{\mathbf{V}} \cdot \nabla \tilde{\mathbf{V}} \right) = -\nabla \cdot p + \nabla \cdot \zeta + \mathbf{J} \times \mathbf{B} - \frac{\mu_{hnf}}{k} \tilde{\mathbf{V}} + (\rho\beta)_{hnf} g (\tilde{T} - \tilde{T}_{\text{ref}}), \quad (2.4)$$

where $\tilde{\mathbf{V}}$ has the components of velocity, \mathbf{B} is the magnetic field, \mathbf{J} is the current density, $\mathbf{J} \times \mathbf{B} = -\sigma_{hnf} B_0^2 \tilde{\mathbf{V}}$, σ_{hnf} is the electrical conductivity of hybrid nanofluid, B_0 is the applied magnetic field, β_{hnf} denotes the thermal expansion coefficient, \tilde{T} is the nanofluid temperature, g is the acceleration due to gravity, T_{ref} is the reference temperature, p is the pressure, ρ_{hnf} represents the density of hybrid nanofluid, k is the porosity parameter, μ_{hnf} is the viscosity of the hybrid nanofluid, hnf in subscript represents the hybrid nanofluid and ζ is the stress

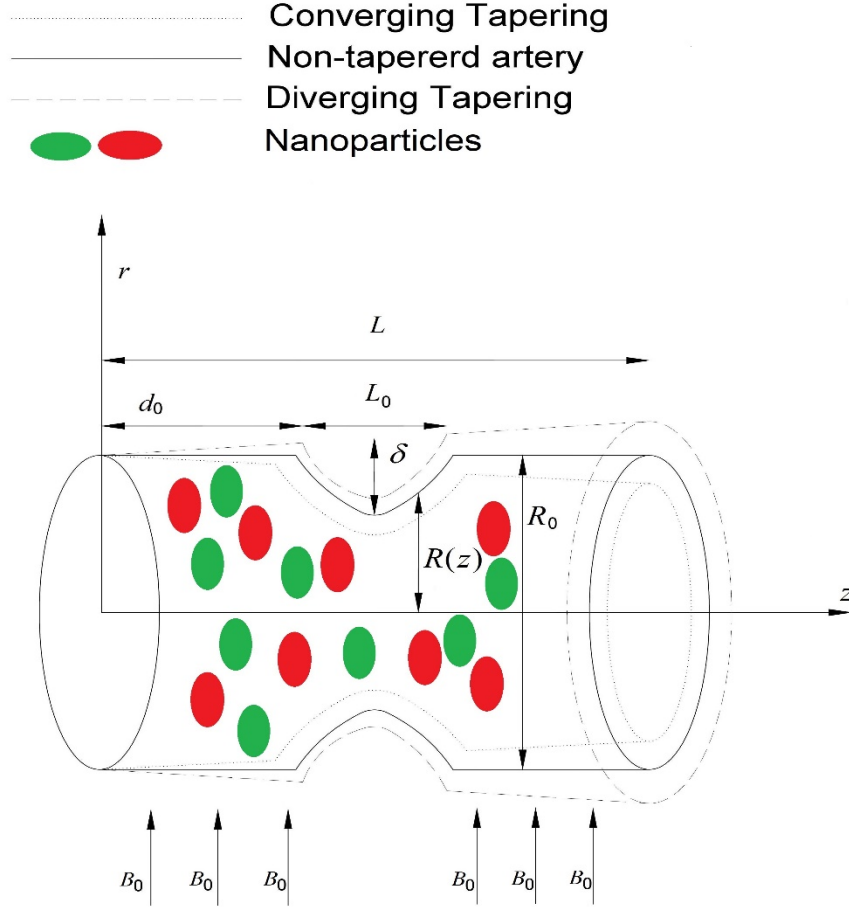


FIGURE 1. Geometrical structure of the blood flow through an anisotropically tapered artery with the suspension of nanoparticles.

tensor for the Williamson fluid model which is defined as [23]:

$$\left. \begin{aligned} \zeta &= \left[\mu_\infty + (\mu_\infty + \mu_{hnf}) (1 - \bar{\gamma}\Gamma)^{-1} \right] \bar{\gamma}, \\ \bar{\gamma} &= \sqrt{\frac{1}{2} \sum_m \sum_n \bar{\gamma}_{mn} \bar{\gamma}_{mn}} = \sqrt{\frac{1}{2} \Pi}, \end{aligned} \right\} \quad (2.5)$$

where μ_∞ is the shear rate viscosity at infinity, Γ the time constant and Π is the second invariant tensor. The expression for the $\mathbf{J} \times \mathbf{B}$ is found as

The temperature equation reads

$$(\rho C_p)_{hnf} \left(\frac{\partial \tilde{T}}{\partial t} + \tilde{\mathbf{V}} \cdot \nabla \tilde{T} \right) = \nabla \cdot (\kappa_{hnf} \nabla \tilde{T}) + \frac{\mathbf{J} \cdot \mathbf{J}}{\sigma_{hnf}} + \zeta \cdot \nabla \tilde{\mathbf{V}} + \varepsilon_0, \quad (2.6)$$

where κ_{hnf} and $(\rho C_p)_{hnf}$ characterize the thermal conductivity and the heat capacity of the hybrid nanofluid, respectively. Also, ε_0 is the heat source ($\varepsilon_0 > 0$)/sink ($\varepsilon_0 < 0$) parameter. The thermo-physical properties of

density, heat capacity, dynamic viscosity, thermal conductivity, thermal expansion coefficient and electric conductivity are defined in the following equations [12, 36]:

i. Density:

$$\begin{aligned}\rho_{nf} &= \rho_f [1 - \Phi_1] + \Phi_1 \rho_{np1}, \\ \rho_{hnf} &= [1 - \Phi_2] \{ \rho_f [1 - \Phi_1] + \Phi_1 \rho_{np1} \} + \Phi_2 \rho_{np2},\end{aligned}\tag{2.7}$$

ii. Heat capacity:

$$\begin{aligned}(\rho C_p)_{nf} &= [1 - \Phi_1] (\rho C_p)_f + \Phi_1 (\rho C_p)_{np1}, \\ (\rho C_p)_{hnf} &= [1 - \Phi_2] \left\{ [1 - \Phi_1] (\rho C_p)_f + \Phi_1 (\rho C_p)_{np1} \right\} + \Phi_2 (\rho C_p)_{np2}.\end{aligned}\tag{2.8}$$

iii. Dynamic viscosity:

$$\begin{aligned}\mu_{nf} &= \frac{\mu_f}{[1 - \Phi_1]^{2.5}}, \\ \mu_{hnf} &= \frac{\mu_f}{[1 - \Phi_1]^{2.5} [1 - \Phi_2]^{2.5}}.\end{aligned}\tag{2.9}$$

iv. Thermal conductivity:

$$\begin{aligned}\kappa_{nf} &= \kappa_f \times \left[\frac{\kappa_{np1} + 2\kappa_f - 2\Phi_1 (\kappa_f - \kappa_{np1})}{\kappa_{np1} + 2\kappa_f + \Phi_1 (\kappa_f - \kappa_{np1})} \right], \\ \kappa_{hnf} &= \kappa_{nf} \times \left[\frac{\kappa_{np2} + 2\kappa_{nf} - 2\Phi_2 (\kappa_{nf} - \kappa_{np2})}{\kappa_{np2} + 2\kappa_{nf} + \Phi_2 (\kappa_{nf} - \kappa_{np2})} \right].\end{aligned}\tag{2.10}$$

v. Thermal expansion coefficient:

$$\begin{aligned}(\rho\beta)_{nf} &= [1 - \Phi_1] (\rho\beta)_f + \Phi_1 (\rho\beta)_{np1}, \\ (\rho\beta)_{hnf} &= [1 - \Phi_2] \left\{ [1 - \Phi_1] (\rho\beta)_f + \Phi_1 (\rho\beta)_{np1} \right\} + \Phi_2 (\rho\beta)_{np2}.\end{aligned}\tag{2.11}$$

vi. Electric conductivity:

$$\begin{aligned}\sigma_{nf} &= \sigma_f \times \left[\frac{\sigma_{np1} (1 + 2\Phi_1) + 2\sigma_f (1 - \Phi_1)}{\sigma_{np1} (1 - \Phi_1) + \sigma_f (2 + \Phi_1)} \right], \\ \sigma_{nhf} &= \sigma_{nf} \times \left[\frac{\sigma_{np2} (1 + 2\Phi_2) + 2\sigma_f (1 - \Phi_2)}{\sigma_{np2} (1 - \Phi_2) + \sigma_f (2 + \Phi_2)} \right].\end{aligned}\tag{2.12}$$

where Φ_1, Φ_2 represent the nanoparticle volume fraction, $np1$ and $np2$ represent the nanoparticles of first (Tantalum) and second (Cobalt) type.

3. LUBRICATION APPROACH

The proposed governing equation can be modelled using lubrication approach. Therefore, to obtain the proposed modeling in dimensionless form, the scaled variables are defined as:

$$\begin{aligned}\tilde{r} &= \frac{r}{R_0}, \tau = \frac{\lambda_0 \tau}{R_0}, \tilde{v} = \frac{\lambda_0}{u_{ave} \delta} v, \tilde{R} = \frac{R}{R_0}, \tilde{p} = \frac{R_0^2}{u_{ave} \lambda_0 \mu} p, \\ \tilde{z} &= \frac{z}{R_0}, T = \frac{\tilde{T} - \tilde{T}_{ref}}{\tilde{T}_1 - \tilde{T}_{ref}}, \tilde{\delta} = \frac{\delta}{R_0}, \lambda = \frac{L}{\lambda_0}, \tilde{u} = \frac{u}{u_{ave}}.\end{aligned}\quad (3.1)$$

where u_{ave} is the averaged velocity of the whole tube over a whole section. Applying equation (3.1) into equations (2.4)–(2.6), we obtain the dimensionless equations as (after ignoring the tilde signs):

$$\frac{\partial p}{\partial z} = \frac{\alpha_1}{r} \frac{\partial}{\partial r} \left[r \frac{\partial u}{\partial r} \left(1 + We \frac{\partial u}{\partial r} \right) \right] - \alpha_2 Ha^2 u - \frac{\alpha_1}{Da} u + Gr \alpha_3 T, \quad (3.2)$$

$$\frac{\alpha_4}{Pr} \frac{1}{r} \frac{\partial}{\partial r} \left(r \frac{\partial T}{\partial r} \right) + \alpha_1 Ec \left(\frac{\partial u}{\partial r} \right)^2 \left(1 + We \frac{\partial u}{\partial r} \right) + \alpha_2 Ec Ha^2 u^2 + \varepsilon, \quad (3.3)$$

where We is the Weissenberg number, Ha is the Hartmann number, Da is the porosity parameter, Gr is the thermal Grashof number, Pr is the Prandtl number, Ec is the Eckert number and ε is the heat source/sink parameter. They are defined as

$$\begin{aligned}We &= \frac{u_{ave} \Gamma}{R_0}, Ha = \sqrt{\frac{\sigma_f}{\mu_f}} B_0 R_0, Da = \frac{k}{R_0^2}, Gr = \frac{(\tilde{T}_1 - \tilde{T}_{ref}) (\rho \beta)_f g R_0^2}{\mu_f u_{ave}}, \\ Pr &= \frac{(\rho C_p)_f v_f}{\kappa_f}, Ec = \frac{u_{ave}^2}{(\tilde{T}_1 - \tilde{T}_{ref}) (C_p)_f}, \varepsilon = \frac{\varepsilon_0 R_0^2}{(\rho C_p)_f v_f (\tilde{T}_1 - \tilde{T}_{ref})},\end{aligned}\quad (3.4)$$

And the reaming parameters $\alpha_1, \alpha_2, \alpha_3, \alpha_4$ are defined as:

$$\alpha_1 = \frac{\mu_{hnf}}{\mu_f}, \alpha_2 = \frac{\sigma_{hnf}}{\sigma_f}, \alpha_3 = \frac{(\rho \beta)_{hnf}}{(\rho \beta)_f}, \alpha_4 = \frac{\kappa_{hnf}}{\kappa_f}, \quad (3.5)$$

The boundary conditions in dimensionless form are defined as:

$$\begin{cases} \frac{\partial u}{\partial r} = \frac{\partial T}{\partial r} = 0 & \text{at } r = 0, \\ u = 0, \theta = 0 & \text{at } r = R. \end{cases} \quad (3.6)$$

4. SERIES SOLUTIONS *via* PERTURBATION APPROACH

To determine the solutions of the nonlinear formulated equations (3.2)–(3.3), we have used the perturbation approach. This perturbation approach was firstly introduced by He [10, 11]. Later, this problem was helpful to solve various nonlinear problems. Let us define the perturbation for the resulting equations (3.2)–(3.3) with

their proposed boundary conditions, we have

$$h(\bar{u}, \bar{\varepsilon}) = (1 - \bar{\varepsilon}) [L(\bar{u}) - L(u_0)] + \bar{\varepsilon} \left[L(\bar{u}) + \frac{We}{r} \left(\frac{\partial \bar{u}}{\partial r} \right)^2 + 2 \frac{\partial \bar{u}}{\partial r} \frac{\partial^2 \bar{u}}{\partial r^2} - \frac{\alpha_2}{\alpha_1} Ha^2 \bar{u} - \frac{1}{Da} \bar{u} + G_r \frac{\alpha_3}{\alpha_1} \bar{T} - \frac{1}{\alpha_1} \frac{dp}{dz} \right], \quad (4.1)$$

$$h(\bar{T}, \bar{\varepsilon}) = (1 - \bar{\varepsilon}) [L(\bar{T}) - L(T_0)] + \bar{\varepsilon} \left[L(\bar{T}) + \frac{\alpha_1 Ec Pr}{\alpha_4} \left\{ \left(\frac{\partial \bar{u}}{\partial r} \right)^2 + We \left(\frac{\partial \bar{u}}{\partial r} \right)^3 \right\} + \frac{Ec Pr \alpha_2}{\alpha_4} Ha^2 \bar{u}^2 + \frac{Pr \bar{\varepsilon}}{\alpha_4} \right], \quad (4.2)$$

where $\bar{\varepsilon}$ represents the artificial embedded parameter.

The following form of linear operator is selected to proceed further

$$L = \frac{1}{r} \frac{\partial}{\partial r} \left(r \frac{\partial}{\partial r} \right). \quad (4.3)$$

In view of equation (3.6) and equation (4.3), the appropriate initial guess is defined as:

$$u_0 = T_0 = \frac{r^2 - R^2}{4}. \quad (4.4)$$

Defining the expansion

$$\bar{u} = \bar{u}_0 + \bar{\varepsilon} \bar{u}_1 + \bar{\varepsilon}^2 \bar{u}_2 + \dots, \quad (4.5)$$

$$\bar{T} = \bar{T}_0 + \bar{\varepsilon} \bar{T}_1 + \bar{\varepsilon}^2 \bar{T}_2 + \dots, \quad (4.6)$$

4.1. Zeroth order system

At zeroth order, we obtain the following set of differential equations

$$L(\bar{u}) - L(u_0) = 0, \quad (4.7)$$

$$L(\bar{T}) - L(\bar{T}_0) = 0, \quad (4.8)$$

The solutions of the above both equations can be written as

$$\bar{u}_0 = \bar{T}_0 = \frac{r^2 - R^2}{4}. \quad (4.9)$$

4.2. First order system

At first order, we obtain the following set of differential equations

$$L(\bar{u}_1) + L(u_0) + \frac{We}{r} \left(\frac{\partial \bar{u}_0}{\partial r} \right)^2 + 2 \frac{\partial \bar{u}_0}{\partial r} \frac{\partial^2 \bar{u}_0}{\partial r^2} - \frac{\alpha_2}{\alpha_1} Ha^2 \bar{u}_0 - \frac{1}{Da} \bar{u}_0 + G_r \frac{\alpha_3}{\alpha_1} \bar{T}_0 - \frac{1}{\alpha_1} \frac{dp}{dz}, \quad (4.10)$$

$$L(\bar{T}_1) + L(T_0) + \frac{\alpha_1 Ec \Pr}{\alpha_4} \left\{ \left(\frac{\partial \bar{u}_0}{\partial r} \right)^2 + We \left(\frac{\partial \bar{u}_0}{\partial r} \right)^3 \right\} + \frac{Ec \Pr \alpha_2}{\alpha_4} Ha^2 \bar{u}_0^2 + \frac{\Pr \varepsilon}{\alpha_4}, \quad (4.11)$$

The solutions of the above both equations can be written as

$$\bar{u}_1 = \frac{1}{192\alpha_1 Da} \left[\begin{aligned} &3(r^2 - R^2) \left(\alpha_1(-16Da + r^2 - 3R^2) + Da \left\{ 16 \frac{dp}{dz} - (\alpha_3 G_r - \alpha_2 Ha^2)(r^2 - 3R^2) \right\} \right) \\ &+ 16\alpha_1 Da(-r^3 + R^3) We \end{aligned} \right], \quad (4.12)$$

$$\bar{T}_1 = \frac{1}{28800\alpha_4} \left[-7200\alpha_4(r^2 - R^2) + \Pr \left\{ \begin{aligned} &-18\alpha_1 Ec(25r^4 + 8r^5 We - R^4(25 + 8RWe)) - 25(r^2 - R^2) \\ &\times (\alpha_2 EcHa^2(2r^4 - 7r^2 R^2 + 11R^4) + 288\varepsilon) \end{aligned} \right\} \right], \quad (4.13)$$

4.3. Second order system

At second order, we obtain the following set of differential equations

$$L(\bar{u}_2) + 2 \frac{We}{r} \frac{\partial \bar{u}_0}{\partial r} \frac{\partial \bar{u}_1}{\partial r} + 2 \frac{\partial}{\partial r} \left(\frac{\partial \bar{u}_0}{\partial r} \frac{\partial \bar{u}_1}{\partial r} \right) - \frac{\alpha_2}{\alpha_1} Ha^2 \bar{u}_1 - \frac{1}{Da} \bar{u}_1 + G_r \frac{\alpha_3}{\alpha_1} \bar{T}_1, \quad (4.14)$$

$$L(\bar{T}_2) + \frac{\alpha_1 Ec \Pr}{\alpha_4} \left\{ 2 \frac{\partial \bar{u}_0}{\partial r} \frac{\partial \bar{u}_1}{\partial r} + 3We \left(\frac{\partial \bar{u}_0}{\partial r} \right)^2 \frac{\partial \bar{u}_1}{\partial r} \right\} + \frac{Ec \Pr \alpha_2}{\alpha_4} Ha^2 \bar{u}_1^2. \quad (4.15)$$

The solutions of the above both equations can be written as

$$\begin{aligned} \bar{u}_2 = & \frac{1}{45158400\alpha_1^2\alpha_4 Da^2} \left[19600\alpha_2\alpha_4 Da^2 Ha^2 (r^2 - R^2) \left(\frac{36 \frac{dp}{dz} (r^2 - 3R^2) - (\alpha_3 G_r - \alpha_2 Ha^2)}{(r^4 - 8r^2 R^2 + 19R^4)} \right) \right. \\ & + 16\alpha_1^2 \left\{ 49\alpha_4 \left(\begin{aligned} &25(r^2 - R^2)(r^4 - 8r^2 R^2 + 19R^4 - 36Da(r^2 - 3R^2)) \\ &+ 48Da(-19r^5 + 50r^3 R^2 + 25r^2 R^3 - 56R^5 + 200Da(r^3 - R^3)) \end{aligned} \right) \right. \\ & \left. \left. \begin{aligned} &We + 3600Da^2(r^4 - R^4)We^2 \\ &+ A3Da^2 Ec G_r \Pr(1225r^6 + 288r^7 We - 441r^2 R^4(25 + 8RWe) + 40R^6(245 + 81RWe)) \end{aligned} \right\} \right. \\ & + 49\alpha_1 Da \left\{ -32\alpha_4 \left(\begin{aligned} &150 \frac{dp}{dz} (-3(r^4 - 4r^2 R^2 + 3R^4) + 32Da(r^3 - R^3)We) + \\ &\alpha_2 Ha^2 \left(\begin{aligned} &-25(r^2 - R^2)(r^4 - 8r^2 R^2 + 19R^4 - 18Da(r^2 - 3R^2)) \\ &+ 24Da(19r^5 - 50r^3 R^2 - 25r^2 R^3 + 56R^5)We \end{aligned} \right) \end{aligned} \right) \right. \\ & \left. + 5\alpha_3 G_r(-80\alpha_4(r^2 - R^2)(r^4 - 8r^2 R^2 + 19R^4 - 36Da(r^2 - 3R^2)) + 768\alpha_4 Da(3r^5 - 10r^3 R^2 + 7R^5) \right. \\ & \left. \left. \times We + 5Da \Pr(r - R)(r + R)(\alpha_2 EcHa^2(r^6 - 7r^4 R^2 + 29r^2 R^4 - 59R^6) + 576(r^2 - 3R^2)\varepsilon) \right) \right] \right], \quad (4.16) \end{aligned}$$

TABLE 1. Thermo-physical features of Blood, Tantalum, and Cobalt nanoparticles [5, 24].

	Blood	Tantalum (Ta)	Cobalt (Co)
ρ (kg/m ³)	3617	16650	8900
κ (W/mK)	0.52	57	100
C_p (J/kg K)	1050	140	445
σ (S/m)	1.33	7.7×10^6	1.7×10^7

$$\begin{aligned}
\bar{T}_2 = & \frac{EcPr}{90316800\alpha_1\alpha_4Da} \left[1225A2DaHa^2 (r^2 - R^2) \left(\frac{-128 \frac{dp}{dz} (2r^4 - 7r^2R^2 + 11R^4) + (\alpha_3G_r - \alpha_2Ha^2)}{(9r^6 - 71r^4R^2 + 181r^2R^4 - 251R^6)} \right) \right. \\
& + 64\alpha_1^2 \left(\frac{-1225 (2r^6 - 9r^4R^2 + 7R^6) - 108 (25r^7 - 98r^5R^2 + 73R^7) We}{+588Da \left(\frac{75r^4 + 96r^5We + 25r^6We^2}{-R^4 (75 + RWe (96 + 25RWe))} \right)} \right) \\
& + \alpha_1 \left\{ \frac{-1225\alpha_2Ha^2 (r^2 - R^2) (9r^6 - 71r^4R^2 + 181r^2R^4 - 251R^6)}{-64Da \left(\alpha_3G_r \left(\frac{-1225 (2r^6 - 9r^4R^2 + 7R^6)}{-108 (25r^7 - 98r^5R^2 + 73R^7) We} \right) \right.} \right. \\
& + 1764 \frac{dp}{dz} (25r^4 + 24r^5We - R^4 (25 + 24RWe)) \\
& \left. \left. + \alpha_2Ha^2 \left(\frac{-2450r^6 + 1500r^7We - 8232r^5R^2We + 3675r^4R^2 (3 + RWe)}{-14700r^2R^4 (3 + RWe) + R^6 (35525 + 17757RWe)} \right) \right) \right\} \right], \tag{4.17}
\end{aligned}$$

The approximate series solutions can be written as

$$u = \lim_{\varepsilon \rightarrow 1} \bar{u} = \bar{u}_0 + \bar{u}_1 + \bar{u}_2 + \dots, \tag{4.18}$$

$$T = \lim_{\varepsilon \rightarrow 1} \bar{T} = \bar{T}_0 + \bar{T}_1 + \bar{T}_2 + \dots, \tag{4.19}$$

The flux (Q) can be computed with the help of following expression

$$Q = \int_0^R 2ru(r, z) dr. \tag{4.20}$$

The expression of impedance can be computed utilizing the above expression (4.20), we have

$$\Gamma = \frac{1}{Q} \int_0^L \left(-\frac{dp}{dz} \right) dz. \tag{4.21}$$

5. RESULTS AND DISCUSSION

In this section, we are going to discuss the plotted results against all the parameters of interest. The results have been computed based on the following parametric values [6, 8]: $\delta = 0.1$, $Da = 0.5$, $Ha = 0.1$, $Pr = 2$, $E_c = 0.1$, $\varepsilon = 1$, $G_r = 0.1$, $We = 0.1$, $\Phi_1 = 0.1$, $\Phi_2 = 0.1$. In addition, Table 1 presents the thermo-physical values of

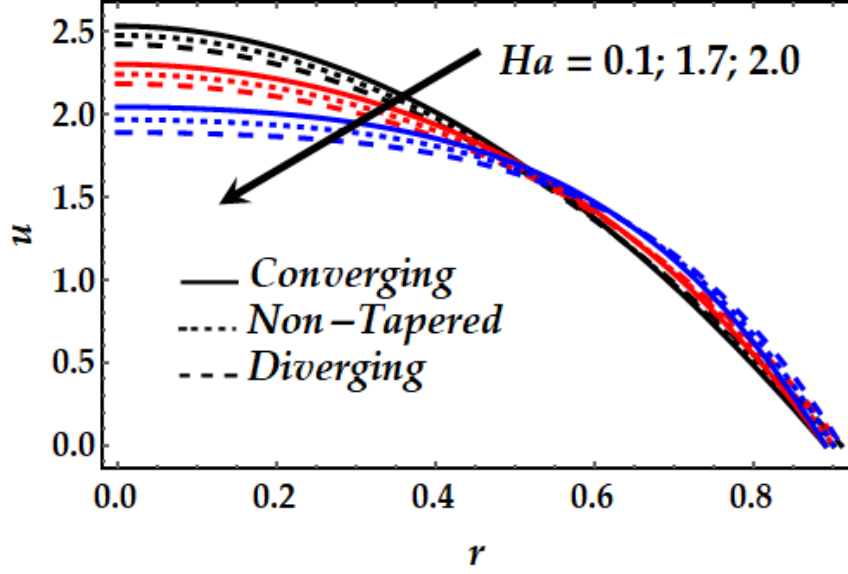


FIGURE 2. Velocity mechanism against multiple values of Hartmann number.

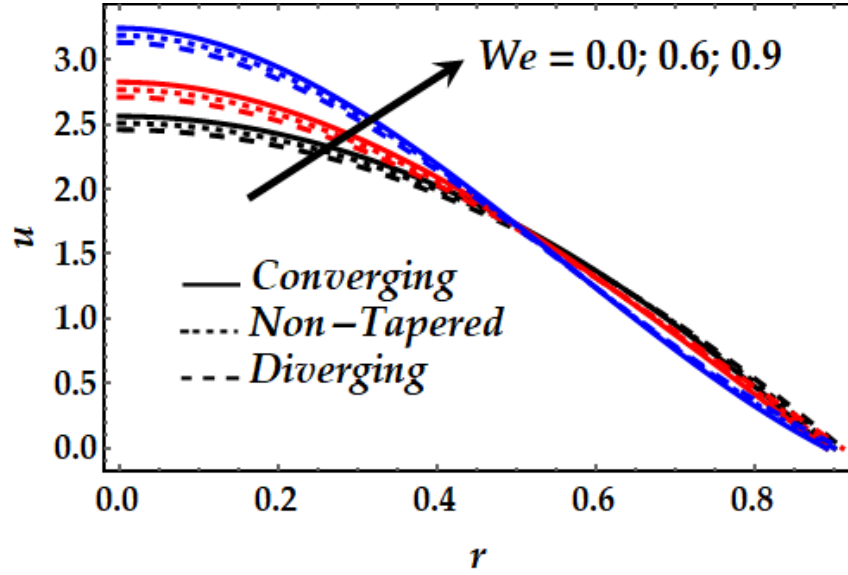


FIGURE 3. Velocity mechanism against multiple values of Weissenberg number.

tantalum, cobalt and blood for experimental and numerical computations. The analytical and numerical results are performed based on the symbolic computational software, Mathematica.

5.1. Velocity mechanism

Figure 2 represents the velocity distribution for various values of Hartmann number Ha for converging, non-tapered and diverging arteries. It is seen that the Hartmann number has a decreasing effect on the velocity profile until $r = 0.45$ from which the behavior is reversed with an increase in Ha . The decrease in the velocity

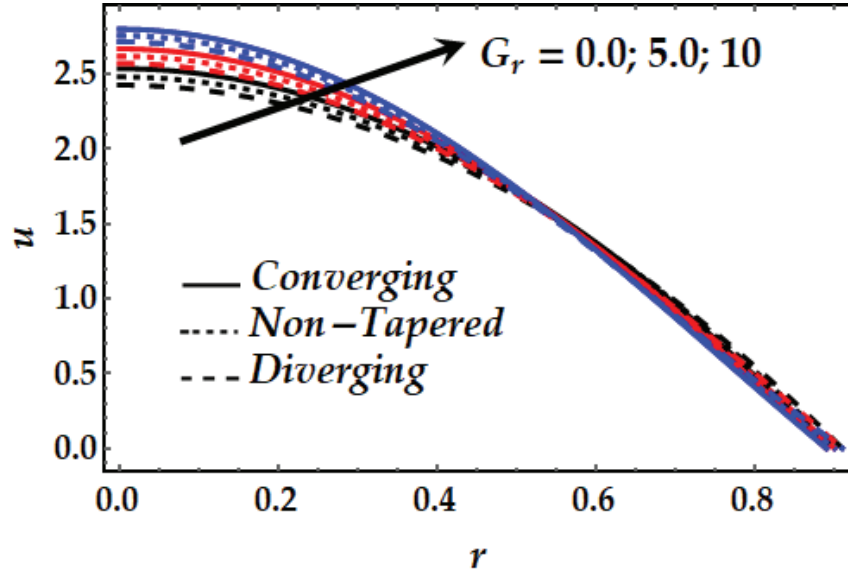


FIGURE 4. Velocity mechanism against multiple values of thermal Grashof number.

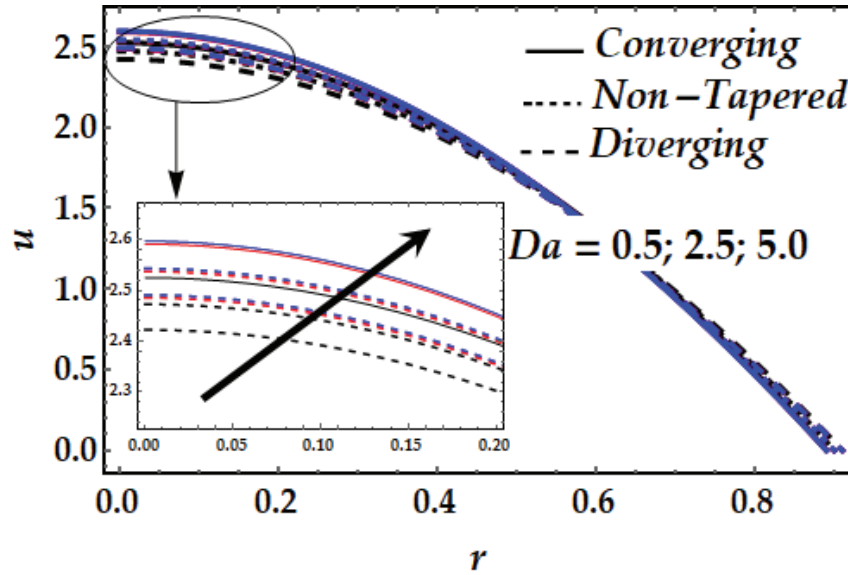


FIGURE 5. Velocity mechanism against multiple values of porosity parameter.

distribution can be attributed to the existence of the Lorentz force that opposes the flow. It is also observed that the flow of the converging artery is accelerated than that of the non-tapered and the diverging ones until almost mid of the artery. The latter behavior is reversed for $r > 0.45$. Figures 3 and 4 depict the velocity profile for progressive values of Weissenberg parameter We (the ratio of the relaxation time of the fluid and a specific process time) and thermal Grashof number Gr . It is observed that both We and Gr enhance the flow till $r = 0.5$ after which the flow is seen decelerating for all types of arteries. It is also seen that the flow of the diverging conduit has least acceleration when compared to the non-tapered and converging ones until the middle of the

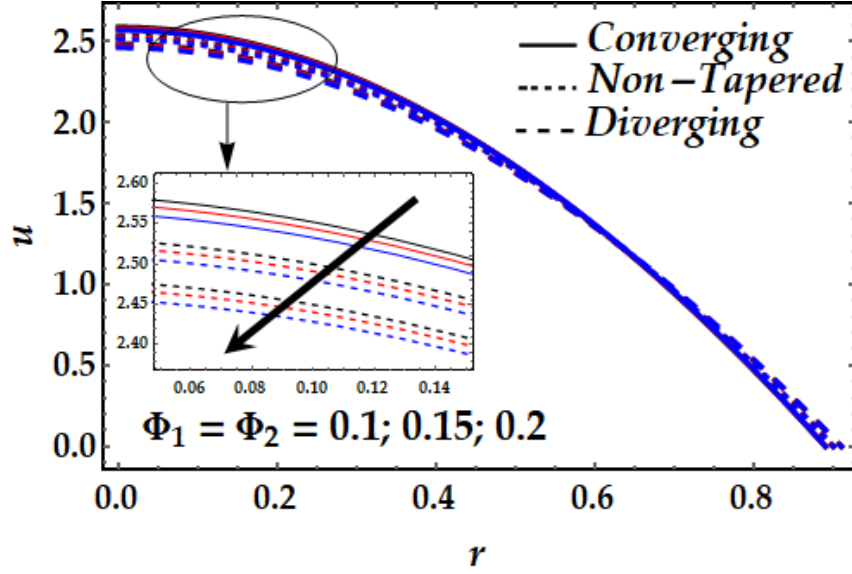


FIGURE 6. Velocity mechanism against multiple values of nanoparticles volume fraction.

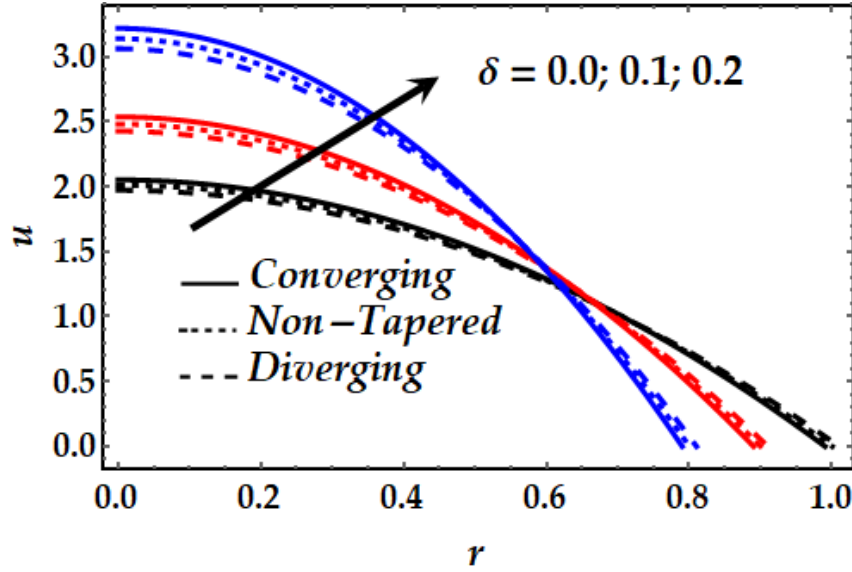


FIGURE 7. Velocity mechanism against multiple values of stenosis height.

conduit before the behavior is reversed near to the walls. It is observed that the results for the Newtonian fluid can be deduced for $We = 0$. Figure 5 is plotted to explain influence of the porosity parameter Da on the velocity mechanism through the conduit. It is seen that the flow profiles for the converging and non-tapered arteries are higher than that of the diverging one. It is observed that Da enhances the flow incrementally for all arteries till almost mid of the conduit after which the behavior is almost negligible. Figure 6 is plotted to examine the distribution of velocity with various values of nanoparticles volume fraction Φ_1 and Φ_2 . It is shown that Φ_1 and Φ_2 have a decreasing effect on the flow in all stenosed segments till midway of the conduit after which

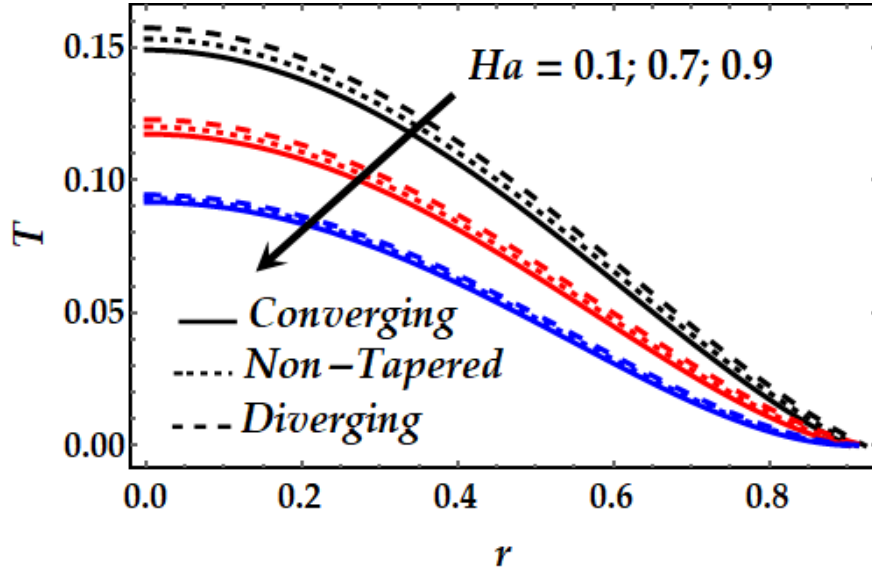


FIGURE 8. Temperature mechanism against multiple values of Hartmann number.

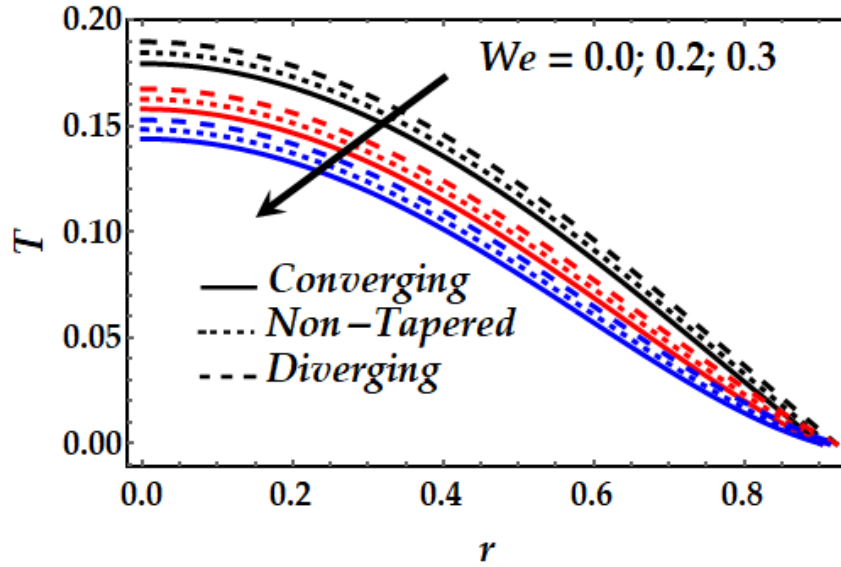


FIGURE 9. Temperature mechanism against multiple values of Weissenberg number.

they weakly affect the flow. Figure 7 depicts the flow mechanism with different values of stenosis height δ . It is noticed that the flow is accelerated with an increase in δ until almost $r = 0.6$ before the behavior is reversed.

5.2. Temperature mechanism

Figures 8–14 show the behavior of temperature distribution against the governing parameters. Figure 8 describes the impact of Ha on the temperature profile for various values of the other parameters. It is seen that the temperature is greatly reduced with enhancing Ha . It is also seen that the temperature of the converging

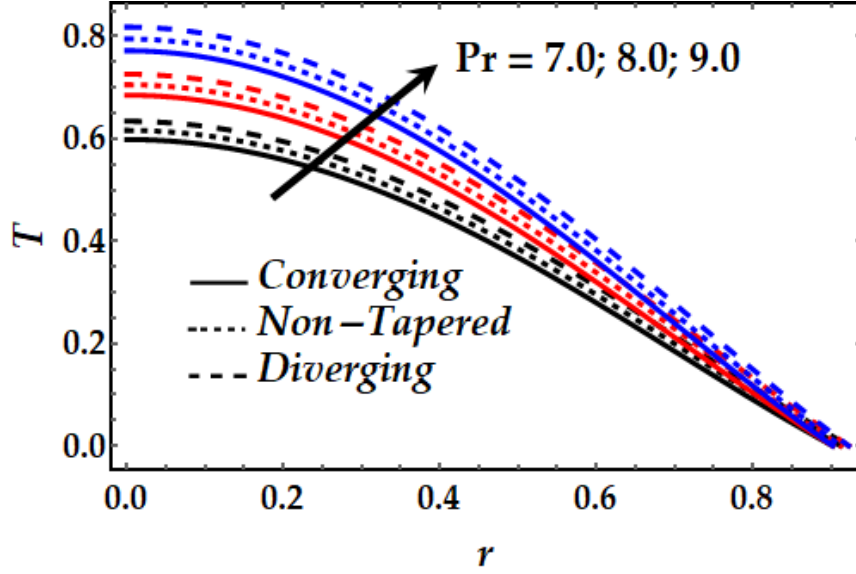


FIGURE 10. Temperature mechanism against multiple values of Prandtl number.

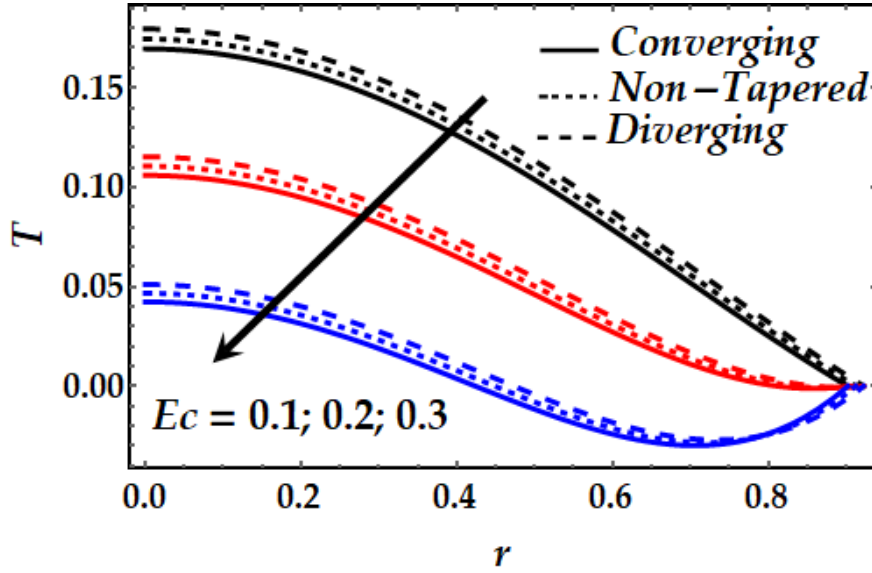


FIGURE 11. Temperature mechanism against multiple values of Eckert number.

conduit is the least among the non-tapered and diverging ones. Figure 9 is plotted to explain the behavior of temperature profile with progressive values of We where it is seen that We has exactly the same effect as Ha . Figure 10 elucidates the effect of Prandtl number Pr on the temperature where it is observed that Pr boosts the temperature across the flow. Figure 11 represents the temperature mechanism with progressive values of Eckert number Ec where it is shown that Ec reduces the temperature steadily across the flow. It is also shown that the temperature of the converging artery is always smaller than that of the non-tapered and diverging ones. Figure 12 depicts the variation of temperature profile with the heat source/sink parameter ε . It is observed that

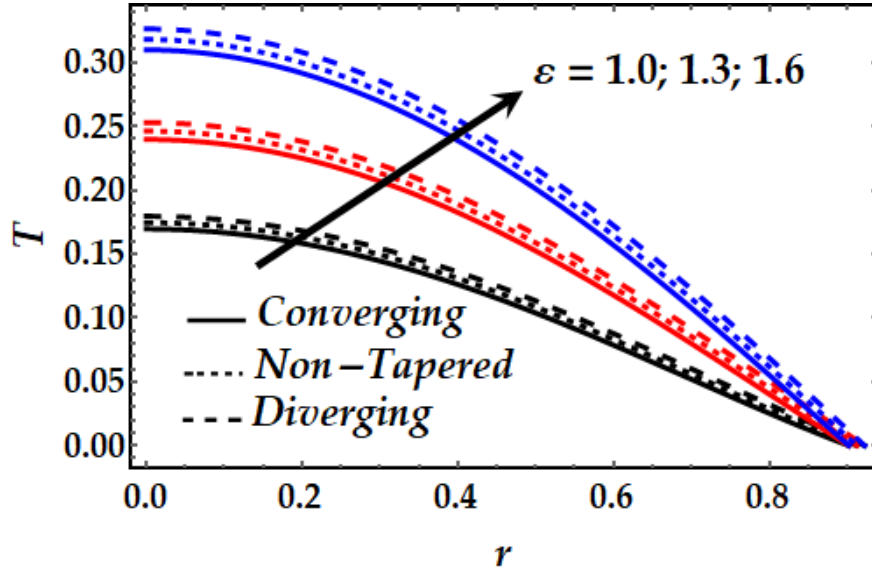


FIGURE 12. Temperature mechanism against multiple values of heat source.

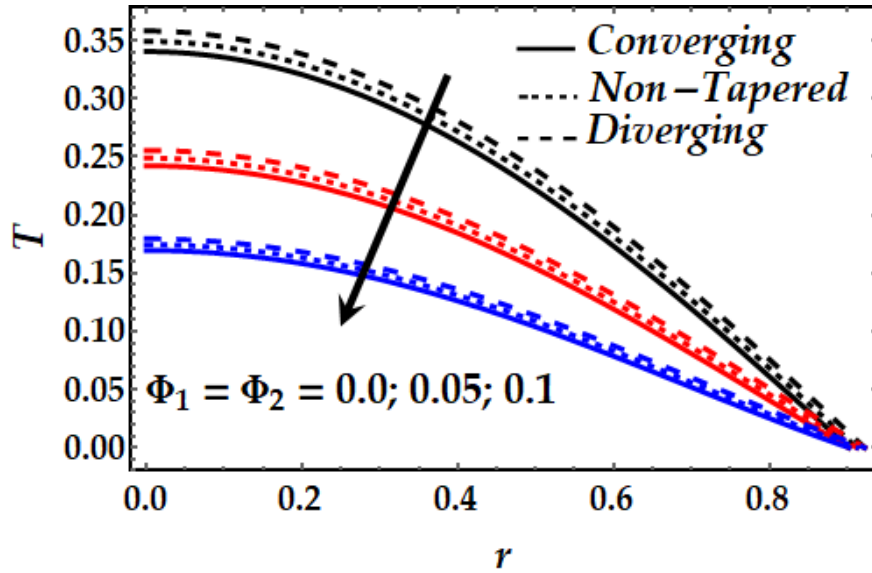


FIGURE 13. Temperature mechanism against multiple values of nanoparticles volume fraction.

the temperature is enhanced with enhancing ε for other values of the parameters under consideration. Inversely, it is noticed from Figures 13 and 14 that Φ_1 , Φ_2 and δ reduce the temperature across the flow greatly.

5.3. Impedance profile

Figures 15 through 19 are plotted to show the behavior of impedance with multiple values of the pertinent parameters of interest. It is seen from Figure 15 that impedance profile is greatly enhanced with an increase in Ha . It is similarly shown in Figure 17 that the impedance has the same exact behavior with δ as it does

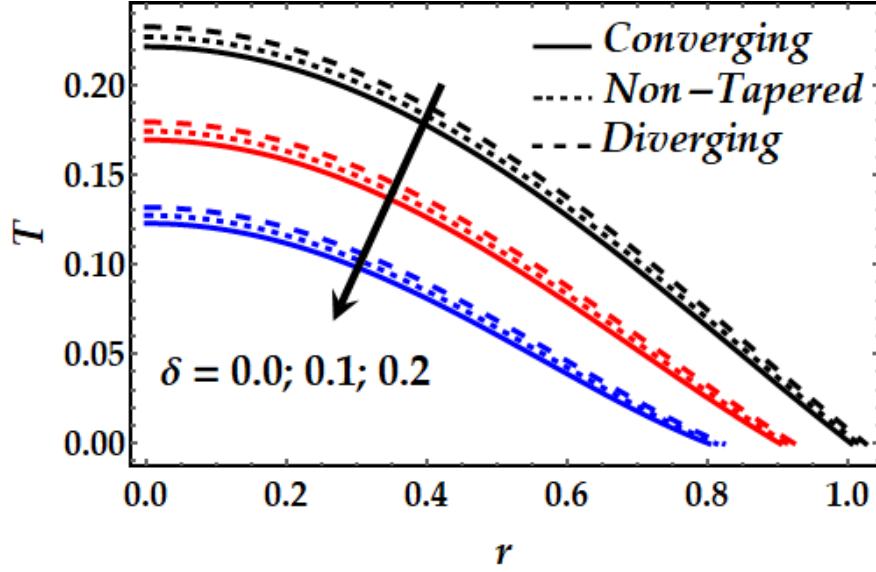


FIGURE 14. Temperature mechanism against multiple values of stenosis height.

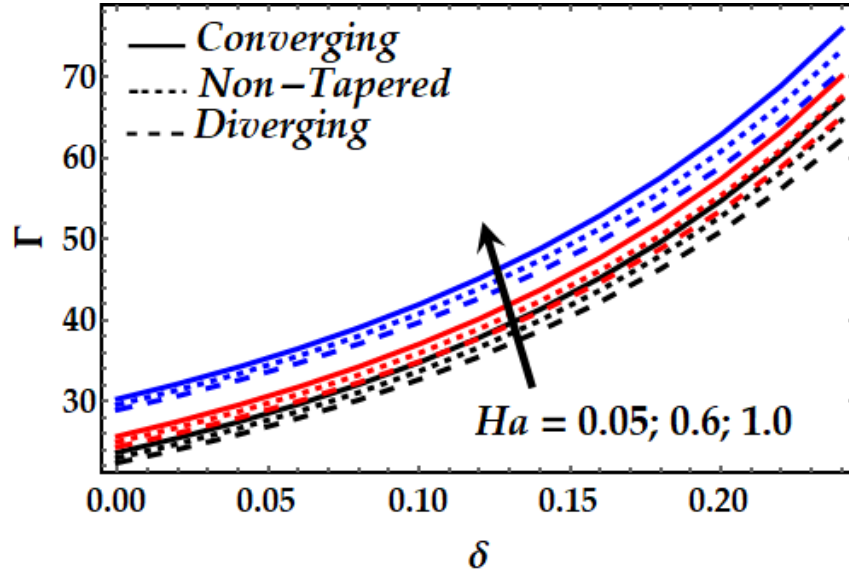


FIGURE 15. Impedance profile against multiple values of Hartmann number.

with Ha . Figures 16 and 18 show the behavior of impedance distribution with progressive values of the porosity parameter Da and the thermal Grashof number Gr . It is noticed that both Da and Gr reduce the impedance steadily all the way for the arteries. It is also seen that the diverging artery's impedance attains the least values than do the converging and non-tapered ones. Figure 19 depicts that Φ_1 and Φ_2 boost the impedance profile greatly. It is generally shown that the impedance profile is higher for the converging artery than that of the non-tapered and diverging ones for any value of the parameters of interest.

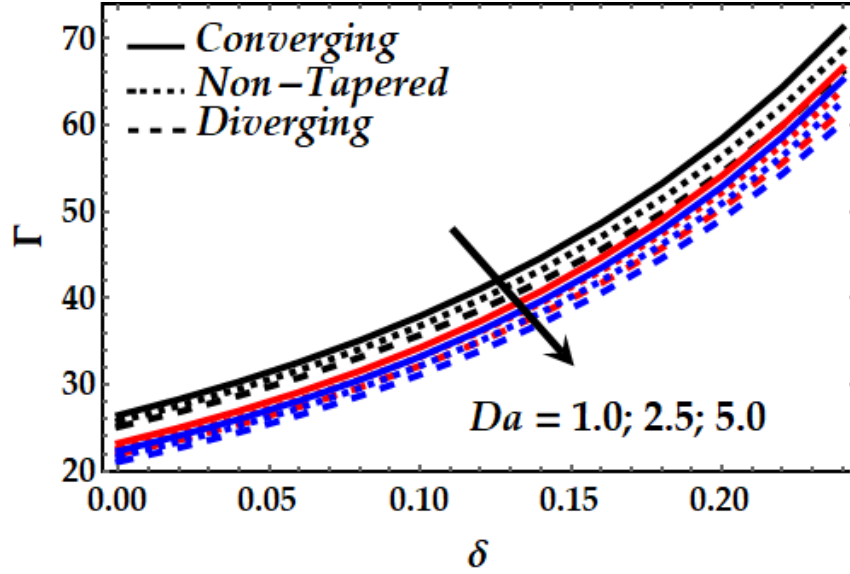


FIGURE 16. Impedance profile against multiple values of porosity parameter.

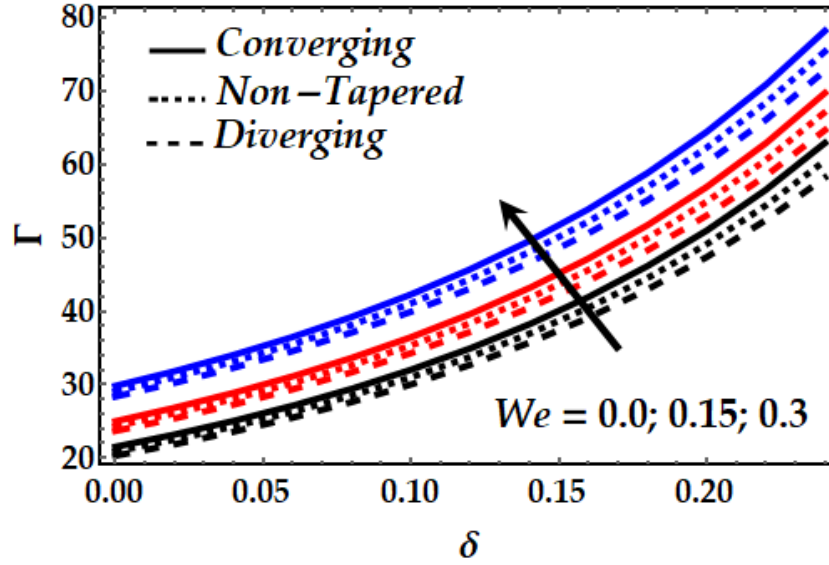


FIGURE 17. Impedance profile against multiple values of Weissenberg number.

5.4. Trapping mechanism

Trapping is an important process in nanofluid flow that may be investigated by visualizing the trajectories. Trapping is the formation of internally flowing free eddies in the blood that are surrounded by streamlines. This process is very important in biology since it aids in the formation of clots in the blood and the pathogenic movement of germs. Figures 20 through 24 are plotted to show the physical effect on streamlines across the flow for various parameters under consideration. It is noticed from Figure 20 that by increasing Da , the number of trapped bolus decreases while the size of bolus is increased. It is observed from Figure 21 that the number trapped

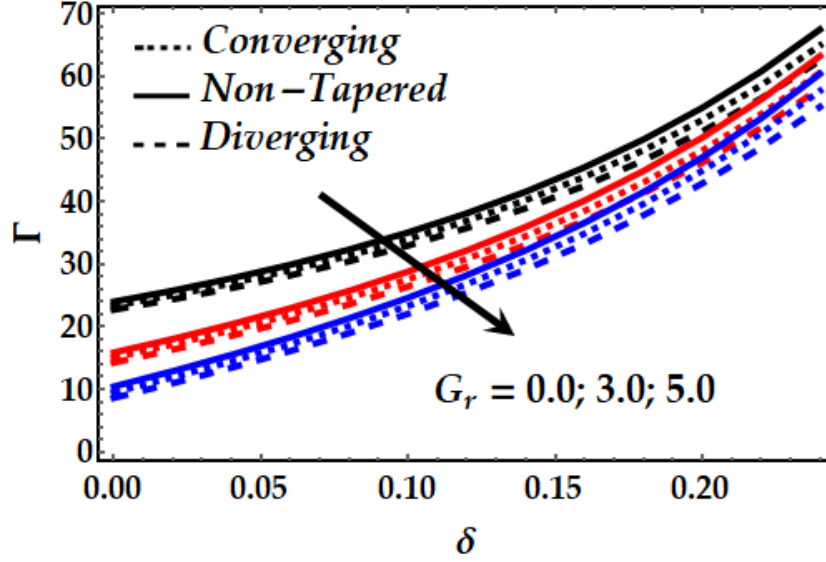


FIGURE 18. Impedance profile against multiple values of thermal Grashof number.

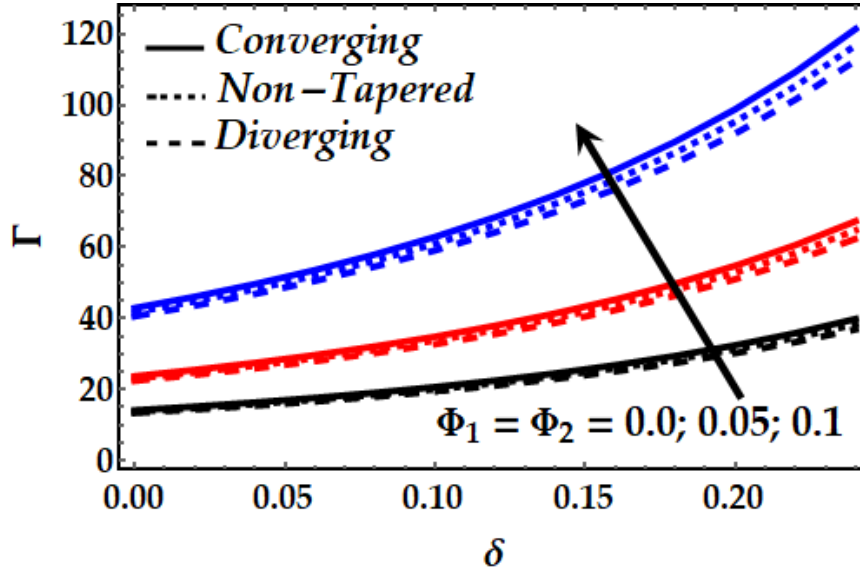


FIGURE 19. Impedance profile against multiple values of nanoparticles volume fraction.

bolus decreases with a decrease in their size by increasing the thermal parameter Gr . Figure 22 shows that the number of trapped bolus increases significantly with an increase in Ha for different values of the pertinent parameters. It is depicted from Figure 23 that the volume fraction reduces the number of trapped bolus greatly. Inversely, it is elucidated from Figure 24 that the tapering angle ϑ decreases the number of trapped bolus in the converging artery and enhances the bolus number in the non-tapered and diverging arteries, respectively.

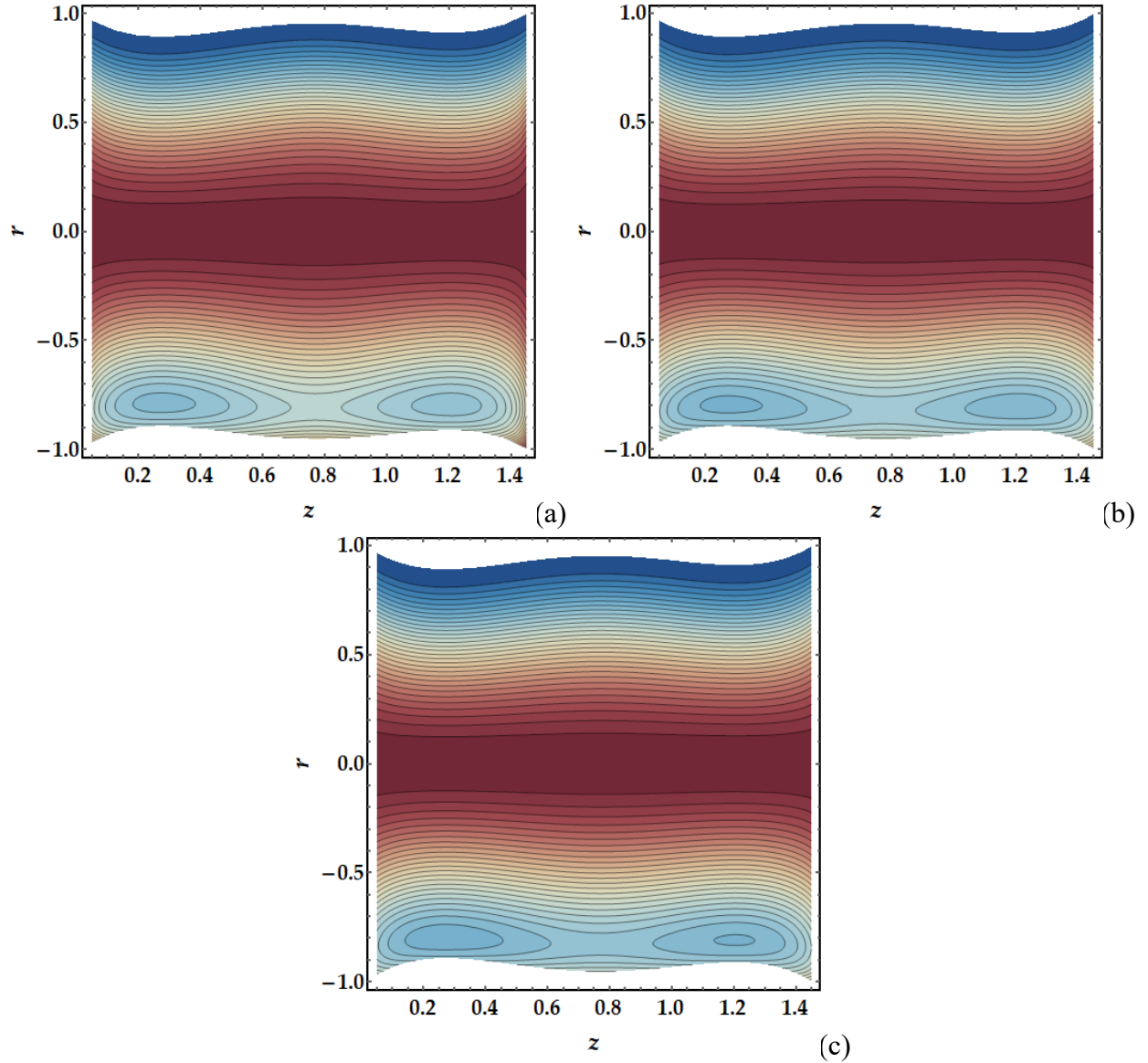


FIGURE 20. Trapping phenomena against multiple values of Porosity parameter (a) 1; (b) 1.5; (c) 2.0.

6. CONCLUSIONS

In the proposed work, we aim to study the effects of cobalt and tantalum nanoparticles embedded in a blood-like fluid presented by a Williamson model through an anisotropically tapered artery. The converging, diverging, and non-tapered arteries' three various geometries are all analyzed. The perturbation method is utilized to obtain the proper solutions of the governing model, whilst the lubrication approach is used to develop the physical and mathematical formulations. Physical interpretation of the impact of the leading parameters are discussed with

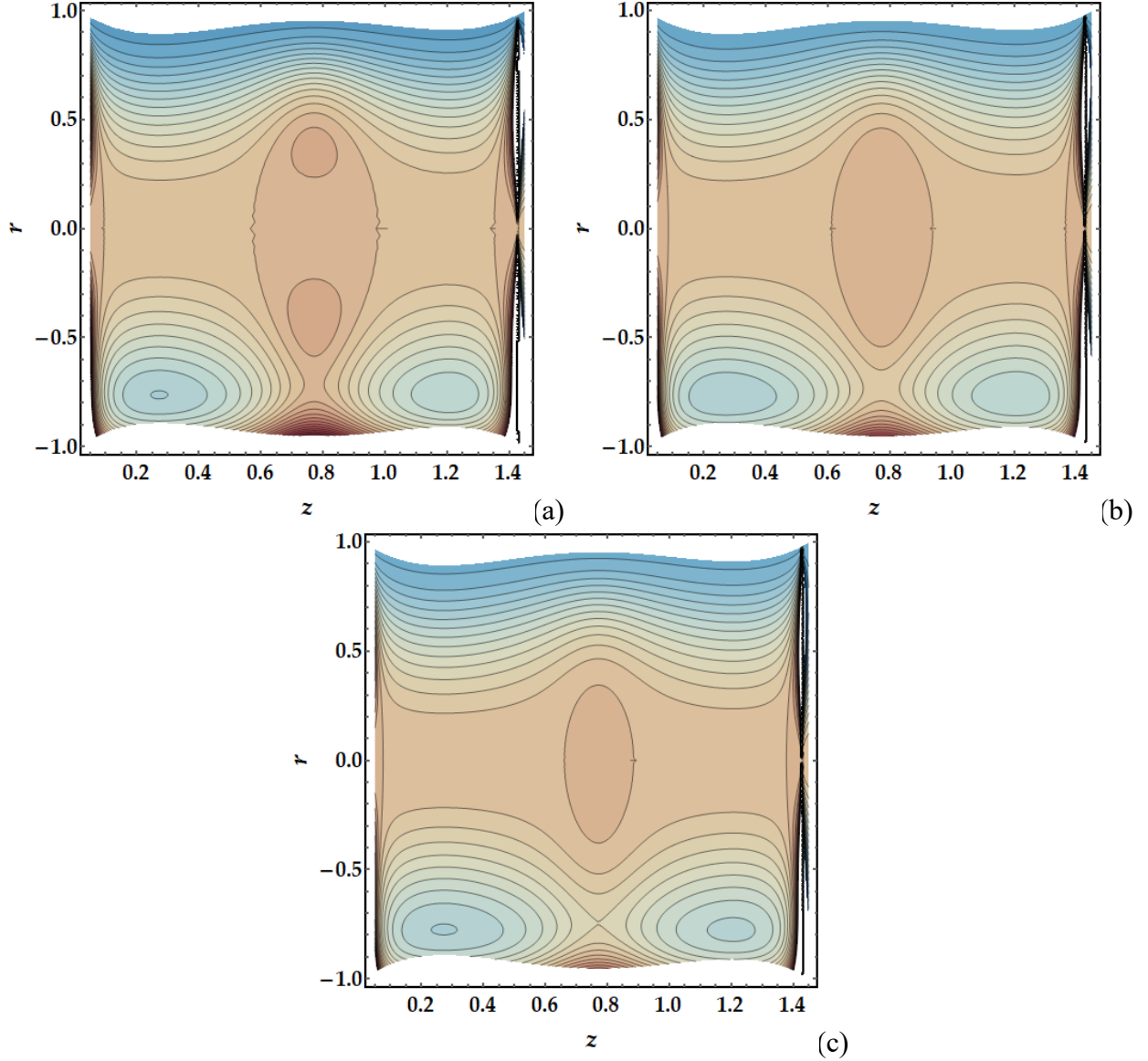


FIGURE 21. Trapping phenomena against multiple values of thermal Grashof number (a) 1; (b) 1.5; (c) 2.0.

the physical variables of interest. The major findings are as follows:

- There is a decrease in velocity due to the existence of Lorentz force.
- The flow of the diverging artery has least acceleration when compared to the non-tapered and converging ones until the middle of the artery.
- The nanoparticles volume fraction reduce the temperature across the flow substantially unlike their impact on the impedance profile.
- The porosity parameter and thermal Grashof number reduce the impedance greatly.
- The number of trapped bolus increases significantly with an increase in the magnetic parameter.

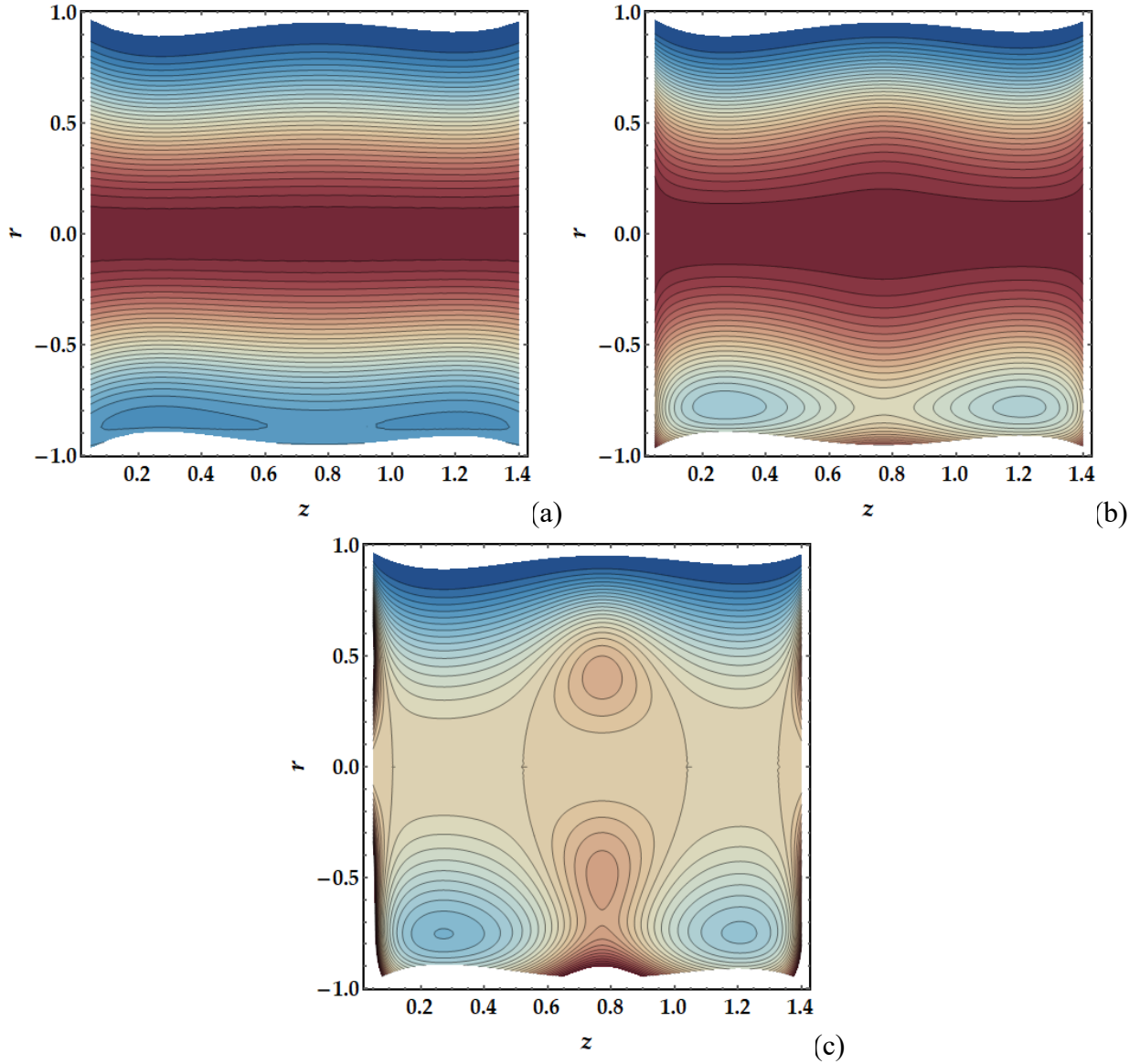


FIGURE 22. Trapping phenomena against multiple values of Hartmann number (a) 0.1; (b) 1.75; (c) 1.9.

- The tapering angle reduces the number of trapped bolus in the converging artery and enhances the bolus number in the non-tapered and diverging arteries.
- Results for the Newtonian fluid can be deduced for $We = 0$.
- The regulation and control of blood mobility at various temperatures may be facilitated by the presence of a magnetic field.

It goes without saying that the use of magnetic NPs is advantageous and fundamental in the treatment of several disorders, including cancer. Magnetic medication delivery and magnetic hyperthermia are two very promising cancer therapy methods. Due to their low toxicity, economic viability, and good biocompatibility,

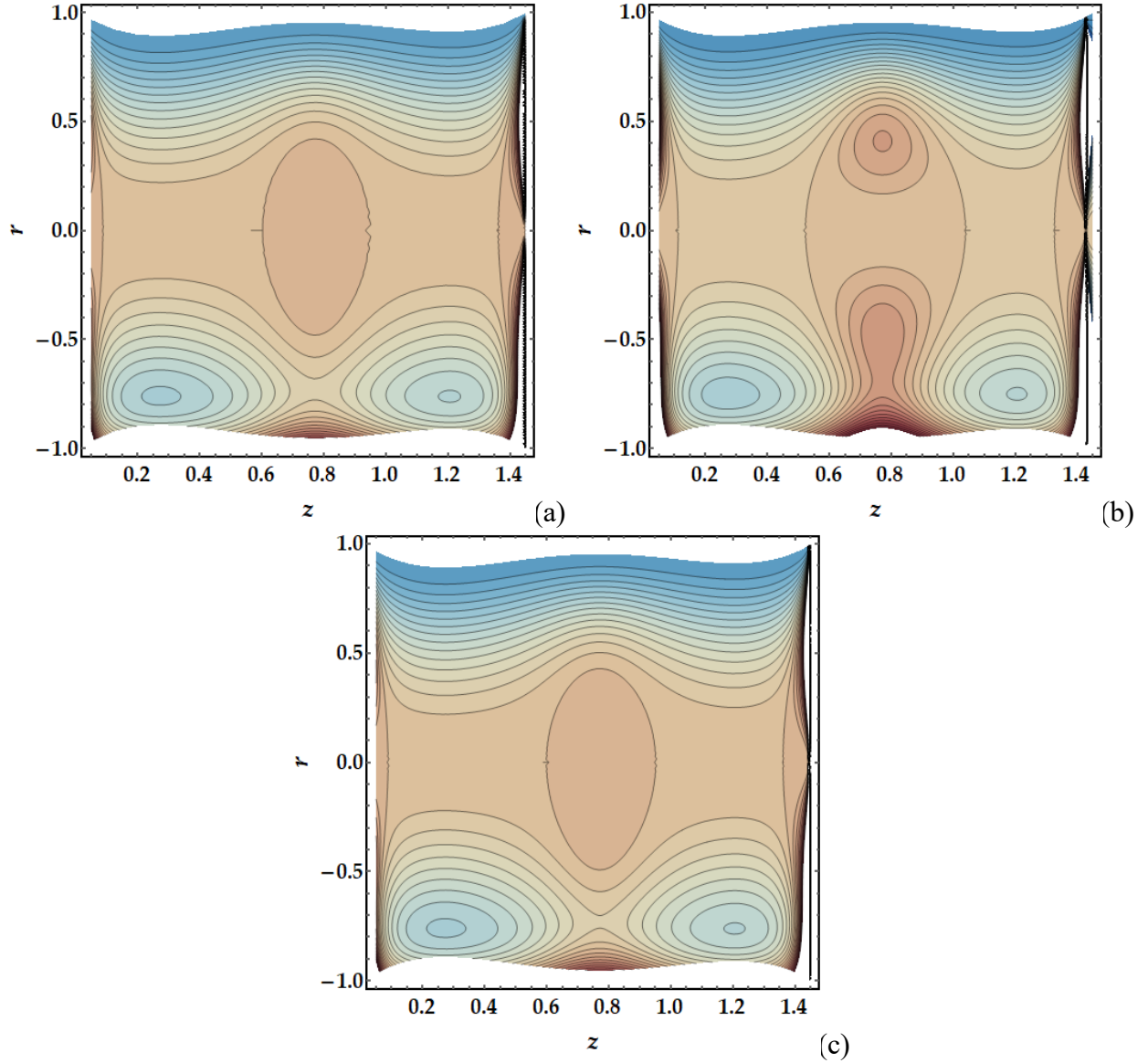


FIGURE 23. Trapping phenomena against multiple values of nanoparticles volume fraction (a) 0; (b) 0.1; (c) 0.2.

cobalt and tantalum nanoparticles offer intriguing biomedical engineering applications. Cobalt and tantalum nanoparticles have arisen in the antibacterial and anticancer fields of medicine, as well as in the treatment of diabetes. However, the restrictions are due to the extrinsic magnetic field's intensity and concerns with tissue penetration, both of which need to be improved. The current findings also illustrate the laminar flow description. The presented results should be helpful for experimental research on heat transfer and non-Newtonian models for magnetized fluid flows.

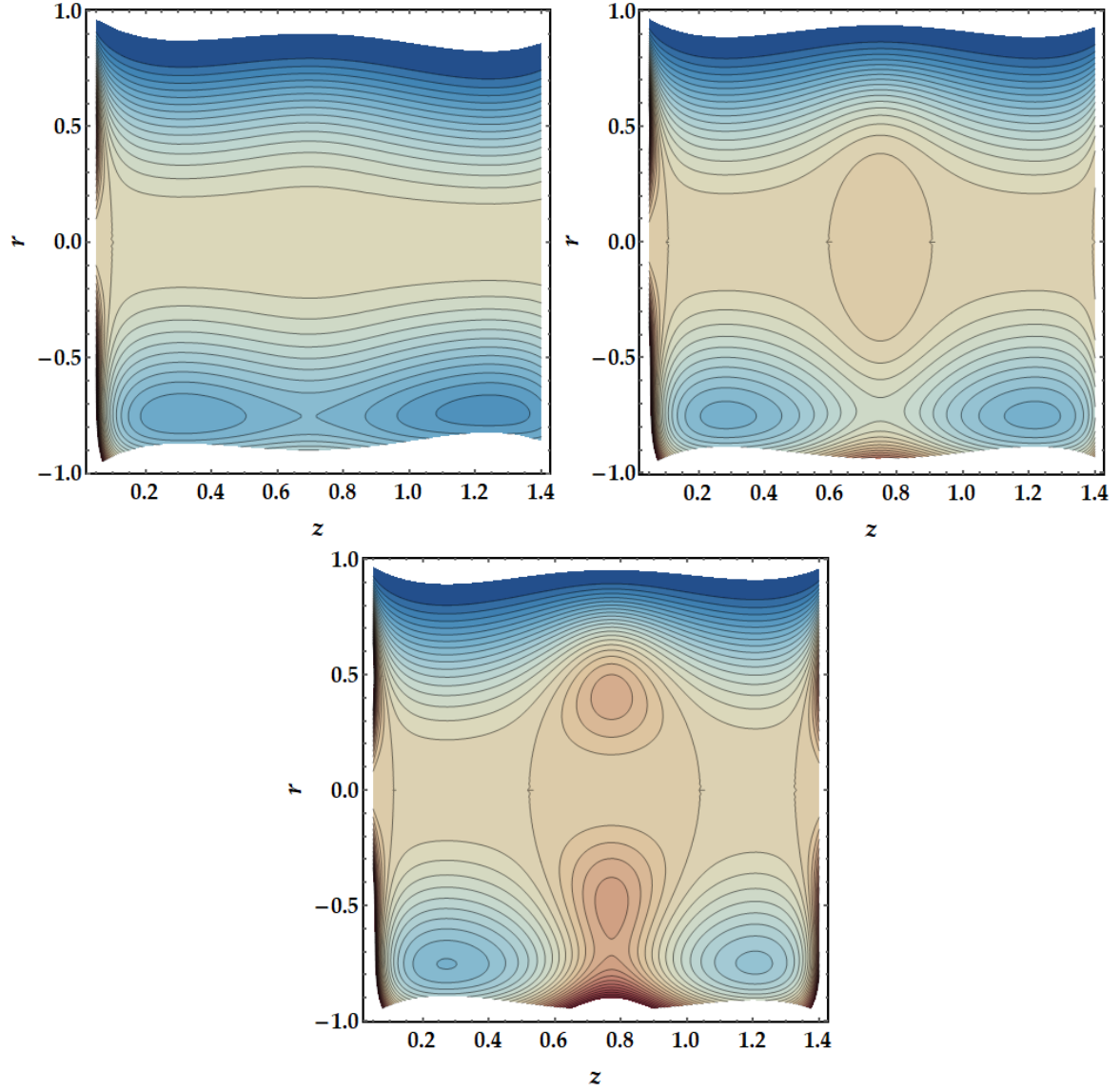


FIGURE 24. Trapping phenomena against multiple values of tapering angle (a) -0.05 ; (b) 0 ; (c) 0.02 .

CONFLICT OF INTEREST/COMPETING INTERESTS

On behalf of all authors, the corresponding author states that there is no conflict of interest.

FUNDING

Not applicable.

Acknowledgements. Sara I. Abdelsalam expresses her deep gratitude to Fundación Mujeres por África for supporting this work through the fellowship awarded to her in 2020.

REFERENCES

- [1] S.I. Abdelsalam and M.M. Bhatti, Anomalous reactivity of thermo-bioconvective nanofluid towards oxytactic microorganisms, *Appl. Math. Mech.* **41** (2020) 711–724.
- [2] S.I. Abdelsalam, J.X. Velasco-Hernández and A.Z. Zaher, Electromagnetically modulated self-propulsion of swimming sperms via cervical canal. *Biomech. Model. Mechanobiol.* **20** (2021) 861–878.
- [3] G. Baldi, D. Bonacchi, C. Innocenti, G. Lorenzi and C. Sangregorio, Cobalt ferrite nanoparticles: the control of the particle size and surface state and their effects on magnetic properties, *J. Magn. Magn. Mater.* **311** (2007) 10–16.
- [4] M.M. Bhatti, S.Z. Alamri, R. Ellahi and S.I. Abdelsalam, Intra-uterine particle-fluid motion through a compliant asymmetric tapered channel with heat transfer, *J. Thermal Anal. Calorim.* **144** (2021) 2259–2267.
- [5] M.M. Bhatti and S.I. Abdelsalam, Bio-inspired peristaltic propulsion of hybrid nanofluid flow with Tantalum (Ta) and Gold (Au) nanoparticles under magnetic effects, *Waves Random Complex Media* (2021) 1–26.
- [6] H.S. Chahregh and S. Dinarvand, TiO₂-Ag/blood hybrid nanofluid flow through an artery with applications of drug delivery and blood circulation in the respiratory system, *Int. J. Numer. Methods Heat Fluid Flow* **30** (2020) 4775–4796.
- [7] S. Dinarvand, Nodal/saddle stagnation-point boundary layer flow of CuO–Ag/water hybrid nanofluid: a novel hybridity model. *Microsyst. Technol.* **25** (2019) 2609–2623.
- [8] R. Ellahi, S.U. Rahman, S. Nadeem and N.S. Akbar, Blood flow of nanofluid through an artery with composite stenosis and permeable walls, *Appl. Nanosci.* **4** (2014) 919–926.
- [9] T. Hayat, S. Ayub, A. Tanveer and A. Alsaedi, Numerical simulation for Mhd Williamson fluid utilizing modified Darcy’s law. *Res. Phys.* **10** (2018) 751–759.
- [10] J.H. He, Homotopy perturbation technique, *Comput. Methods Appl. Mech. Eng.* **178** (1999) 257–262.
- [11] J.H. He, Homotopy perturbation method: a new nonlinear analytical technique, *Appl. Math. Comput.* **135** (2003) 73–79.
- [12] B. Jabbaripour, N.M. Rostami, S. Dinarvand and I. Pop, Aqueous aluminium–copper hybrid nanofluid flow past a sinusoidal cylinder considering three-dimensional magnetic field and slip boundary condition, *Proc. Inst. Mech. Eng. E* (2021) 09544089211046434.
- [13] M.Y. Malik and T. Salahuddin, Numerical solution of Mhd stagnation point flow of Williamson fluid model over a stretching cylinder, *Int. J. Nonlinear Sci. Numer. Simul.* **16** (2015) 161–164.
- [14] Z.H. Miao, P.Y. Liu, Y.C. Wang, K. Li, D.D. Huang, H.J. Yang, Q.L. Zhao, Z.B. Zha, L. Zhen and C.-Y. Xu, Pegylated tantalum nanoparticles: a metallic photoacoustic contrast agent for multiwavelength imaging of tumors. *Small* **15** (2019) 1903596.
- [15] G. Mohandas, N. Oskolkov, M.T. McMahon, P. Walczak and M. Janowski, Porous tantalum and tantalum oxide nanoparticles for regenerative medicine, *Acta Neurobiolog. Exp. (Wars)* **74** (2014) 188–196.
- [16] N. Moumen, P. Veillet and M.P. Pileni, Controlled preparation of nanosize cobalt ferrite magnetic particles, *J. Magn. Magn. Mater.* **149** (1995) 67–71.
- [17] S.M. Mousavi, M.N. Rostami, M. Yousefi, S. Dinarvand, I. Pop and M.A. Sheremet, Dual solutions for Casson hybrid nanofluid flow due to a stretching/shrinking sheet: a new combination of theoretical and experimental models, *Chin. J. Phys.* **71** (2021) 574–588.
- [18] S. Nadeem and S. Akram, Influence of inclined magnetic field on peristaltic flow of a Williamson fluid model in an inclined symmetric or asymmetric channel. *Math. Comput. Modell.* **52** (2010) 107–119.
- [19] T. Neuberger, B. Schöpf, H. Hofmann, M. Hofmann and B.V. Rechenberg, Superparamagnetic nanoparticles for biomedical applications: possibilities and limitations of a new drug delivery system, *J. Magn. Magn. Mater.* **293** (2005) 483–496.
- [20] A.T. Ngo, P. Bonville and M.P. Pileni, Nanoparticles of Co_xFe_yD_zO₄: synthesis and superparamagnetic properties, *Eur. Phys. J. B* **9** (1999) 583–592.
- [21] A.S. Ponce, E.F. Chagas, R.J. Prado, C.H.M. Fernandes, A.J. Terezo and E. Baggio-Saitovitch, High coercivity induced by mechanical milling in cobalt ferrite powders. *J. Magn. Magn. Mater.* **344** (2013) 182–187.
- [22] J. Prakash, N. Balaji, E.P. Siva and A.D. Chanrasekaran, Non-linear blood flow analysis on Mhd peristaltic motion of a Williamson fluid in a micro channel. *AIP Conf. Proc.* **2112** (2019) 020048–10.
- [23] B.M.J. Rana, S.M. Arifuzzaman, S. Islam, E-S. Reza-Rabbi, A. Al-Mamun, M. Mazumder, K.C. Roy and M.S. Khan, Swimming of microbes in blood flow of nano-bioconvective Williamson fluid, *Thermal Sci. Eng. Progr.* **25** (2021) 101018.
- [24] M.N. Rashin and J. Hemalatha, Magnetic and ultrasonic studies on stable cobalt ferrite magnetic nanofluid, *Ultrasonics* **54** (2014) 834–840.
- [25] R. Raza, F. Mabood, R. Naz and S.I. Abdelsalam, Thermal transport of radiative Williamson fluid over stretchable curved surface, *Therm. Sci. Eng. Progr.* **23** (2021) Article 100887.
- [26] T. Ren, R. Tran, S. Lee, A. Bandera, M. Herrera, X. Li, S.P. Ong and O.A. Graeve, Morphology control of tantalum carbide nanoparticles through dopant additions, *J. Phys. Chem. C* **125** (2021) 10665–10675.
- [27] A. Saleem, S. Akhtar and S. Nadeem, Bio-mathematical analysis of electro-osmotically modulated hemodynamic blood flow inside a symmetric and nonsymmetric stenosed artery with joule heating, *Int. J. Biomath.* **15** (2022) 2150071.
- [28] S.A. Salman, T. Usami, K. Kuroda and M. Okido, Synthesis and characterization of cobalt nanoparticles using hydrazine and citric acid, *J. Nanotechnol.* **2014** (2014) Article ID 525193, 6 pages.
- [29] J. Schoon, S. Geißler, J. Traeger, A. Luch, J. Tentschert, G. Perino, F. Schulze, G.N. Duda, C. Perka and A. Rakow, Multi-elemental nanoparticle exposure after tantalum component failure in hip arthroplasty: in-depth analysis of a single case, *Nanomedicine* **13** (2017) 2415–2423.

- [30] K. Subbarayudu, S. Suneetha and P. Bala Anki Reddy, The assessment of time dependent flow of Williamson fluid with radiative blood flow against a wedge, *Propuls. Power Res.* **9** (2020) 87–99.
- [31] T.A. Tabish, M.N. Ashiq, M.A. Ullah *et al.*, Biocompatibility of cobalt iron oxide magnetic nanoparticles in male rabbits, *Korean J. Chem. Eng.* **33** (2016) 2222–2227.
- [32] L.D. Tung, V. Kolesnichenko, D. Caruntu, N.H. Chou, C.J. O’connor and L. Spinu, Magnetic properties of ultrafine cobalt ferrite particles, *J. Appl. Phys.* **93** (2003) 7486–7488.
- [33] A. Waris, M. Din, A. Ali, S. Afridi, A. Baset, A.U. Khan and M. Ali, Green fabrication of Co and Co₃O₄ nanoparticles and their biomedical applications: a review, *Open Life Sci.* **16** (2021) 14–30.
- [34] M. Zeisberger, S. Dutz, R. Müller, R. Hergt, N. Matoussevitch and H. Bönemann, Metallic cobalt nanoparticles for heating applications, *J. Magn. Magn. Mater.* **311** (2007) 224–227.
- [35] L. Zhang, E. Haddouti, H. Beckert, R. Biehl, S. Pariyar, J.M. Rüwald, X. Li, M. Jaenisch, C. Burger, D.C. Wirtz, K. Kabir and F.A. Schildberg, Investigation of cytotoxicity, oxidative stress, and inflammatory responses of tantalum nanoparticles in Thp-1-derived macrophages. *Med. Inflamm.* **2020** (2020) ARTICLE ID 3824593.
- [36] L. Zhang, M.M. Bhatti, E.E. Michaelides, M. Marin and R. Ellahi, Hybrid nanofluid flow towards an elastic surface with tantalum and nickel nanoparticles, under the influence of an induced magnetic field, *Eur. Phys. J. Special Topics* **231** (2022) 521–533.
- [37] A.M. Zidan, L.B. Mccash, S. Akhtar, A. Saleem, A. Issakhov and S. Nadeem, Entropy generation for the blood flow in an artery with multiple stenosis having a catheter. *Alexandr. Eng. J.* **60** (2021) 5741–5748.



Please help to maintain this journal in open access!

This journal is currently published in open access under the Subscribe to Open model (S2O). We are thankful to our subscribers and supporters for making it possible to publish this journal in open access in the current year, free of charge for authors and readers.

Check with your library that it subscribes to the journal, or consider making a personal donation to the S2O programme by contacting subscribers@edpsciences.org.

More information, including a list of supporters and financial transparency reports, is available at <https://edpsciences.org/en/subscribe-to-open-s2o>.